High-precision digital terahertz phase manipulation within a multichannel field perturbation coding 2DEG meta-chip

Hongxin Zeng
University of Electronic Science and Technology of China https://orcid.org/0000-0002-4404-9485
Huajie Liang
University of Electronic Science and Technology of China
Yaxin Zhang (zhangyaxin@uestc.edu.cn)
University of Electronic Science and Technology of China
Ziqiang Yang
University of Electronic Science and Technology of China
Feng Lan
University of Electronic Science and Technology of China
Shixiong Liang
Hebei Semiconductor Research Institute
Zheng Li
University of Electronic Science and Technology of China
Lan Wang
University of Electronic Science and Technology of China
Xilin Zhang
University of Electronic Science and Technology of China
Sen Gong
University of Electronic Science and Technology of China
Yubin Gong
University of Electronic Science and Technology of China
Ziqiang Yang
University of Electronic Science and Technology of China

Article

Keywords: Metamaterials, Electronic Transport Characteristics, Perturbation Resonances

Posted Date: October 28th, 2020

DOI: https://doi.org/10.21203/rs.3.rs-92448/v1

Version of Record: A version of this preprint was published at Nature Photonics on August 9th, 2021. See the published version at https://doi.org/10.1038/s41566-021-00851-6.

Abstract

Terahertz phase manipulation has always been based on direct coupling of the resonance of quasi-optical terahertz waves with metamaterials, which is accompanied by unnecessary amplitude modulation, thus limiting the accuracy of phase manipulation and its application in monolithic integrated systems. Here, we propose a coding meta-chip composed of transmission lines and two-dimensional electron gas (2DEG) meta-atoms, wherein local perturbation resonances are induced to manipulate the phase of terahertz waves. By controlling the electronic transport characteristics of the 2DEG with external voltages, the intensity of the perturbation can be manipulated, which affects the transmission phase of the waves. More importantly, the perturbation resonances induced by different meta-atoms can be coupled so that through digital coding of the perturbation state of 2DEG meta-atoms, the terahertz wave transmission phase can be manipulated with high precision. As a result, phase manipulation with different precisions from 2° to 5° is observed from 0.26 to 0.27 THz, where the average phase error is only 0.36°, and the maximum root mean square of the transmittance is 0.36 dB. This high-precision phase manipulation via field coding has great application potential in the fields of beamforming, wireless communication, and high-resolution imaging.

Introduction

Terahertz (THz) technology has potentially transformative applications in high-rate communication, biomedical imaging, holography, spectroscopy, radar and security[1–13]. As the demand for the wireless bandwidth increases, wireless communication systems applying terahertz waves as carriers provide ultrahigh transmission rates and low delays, which are expected to exceed those of 5G communication systems. The demand for terahertz systems is driving the development of high-performance integrated terahertz devices. As one of the key techniques, the efficient and dynamic manipulation of the phase and amplitude of THz waves has to become the subject of in-depth research worldwide. The dynamic metamaterials composed of a metamaterial and an active material have led to remarkable achievements in terahertz amplitude and phase dynamic manipulation devices[4,14–21]. The resonance mode and intensity of such metamaterials are affected by the distribution of electrons in the metamaterial structure. Different transport paths of electrons generate various resonance modes, such as LC resonance[14], dipole resonance[21], and Fano resonance[16]. Metamaterials containing active materials can transform the electrical characteristics under external excitation, altering the resonance mode and intensity to manipulate terahertz waves.

As early as 2006, the combination of metamaterials and doped semiconductors realized the modulation

of the terahertz wave transmission amplitude for the first time[14]. Since then, various THz dynamic or tunable metamaterials have emerged to achieve effective manipulation of the THz wave amplitude and phase[22–31]. In 2009, a composite metamaterial based on an n-doped GaAs layer was reported[22], which achieved a phase modulation of 0.56 rad. Subsequently, doped silicon[24], vanadium oxide[29], graphene[25,32], high electron mobility transistors (HEMTs)[30], liquid crystals[33], and other dynamic materials were used to manipulate the terahertz wave phase, promoting the development of terahertz phase manipulation devices. However, almost all terahertz phase manipulation devices with dynamic metamaterials are based on the direct interaction between terahertz waves and metamaterials, which results in sensitivity of the phase to the resonant mode and intensity and affects the linearity and accuracy of the phase manipulation. Furthermore, general dynamic metamaterial phase-controlling devices work in free space, which is not the case for integrated systems.

To overcome the above issues, the development of THz phase dynamic manipulation requires a completely new mechanism. Instead of coupling all of the terahertz wave with the metamaterial, coupling a minority of the energy of the terahertz wave with the metamaterial may improve the phase manipulation accuracy and reduce system losses. Interacting with on-chip terahertz waves, instead of with free space terahertz waves, may enable convenient integration of the system.

Recently, an information metamaterial[34–41], as a special digital metamaterial, consisting of coding meta-atoms digitalized as “0” or “1” was introduced. The binary codes produce different effects on electromagnetic waves by varying the electromagnetic characteristics of the meta-atoms. In this way, digital metamaterials can be programmed to realize numerous functions, such as communication[40], imaging[35,36] and holography[34]. These works suggest that phase manipulation can be programmed with different coding sequences to achieve a precise degree of phase shifting. This approach also possesses great advantages in high-rate and real-time systems. Based on these considerations, in this paper, a multichannel field perturbation coding 2DEG meta-chip (MPCM) combining nanometer 2DEG meta-atoms and on-chip transmission lines is proposed. Different from the general dynamic metamaterial structure, the meta-atom is not directly coupled with all of the terahertz wave in free space but with a minority of the terahertz wave on the chip to form a local resonance perturbing the quasi-TEM terahertz wave on the chip. By controlling the electronic transport in 2DEG nanostructures, the perturbation intensity is altered to shift the phase. In addition, coding the perturbation intensity generated by different meta-atoms results in diverse perturbations with different orders to finely manipulate the THz phase.

The MPCM that we propose, as shown in fig. 1, combines an on-chip microstrip transmission line with meta-atoms. As a main transmission line, the on-chip microstrip line divides the surface of the substrate into two sides: on one side is placed 2DEG nanostructures, and the other side has a grounded metal pad. All of the metal layers are 1 μm thick gold, which are fabricated on a 50 μm thick SiC substrate. The meta-atom consists of one metal pad, one gaped thin metal line, and two metal electrodes located on both sides of the gap. The 2DEG, which use the same manufacturing processes as HEMTs, is nested in the gap, providing active properties to the device. A terahertz wave propagates along the main transmission

line, wherein the energy is concentrated in the dielectric substrate. The electric fields of the on-line propagating terahertz wave can induce weak resonant modes in the unilaterally located meta-atoms; meanwhile, the change in the transport of the 2DEG in the meta-atom causes a variation in the carrier concentration, which leads to a further change in the electronic stacking in both metal electrodes. Such a change in the electronic stacking can generate different perturbations of the electromagnetic field distributed on the surface of the substrate and cause a phase shift of the terahertz wave transmitting along the main transmission line. With this mechanism, we can consider that in the case of a high carrier concentration of the 2DEG, named the “0” state, a slight electronic stacking occurs in both metal electrodes of the meta-atoms, which brings about a high concentration 2DEG resonance (HCR) for the terahertz wave. The HCR leads to a faint perturbation of the electromagnetic field. In the contrary case, named the “1” state, the low carrier concentration of the 2DEG allows more electronic stacking in both metal electrodes, which means a depleted 2DEG resonance (DR) can be produced, which slightly enhances the perturbation to a mild perturbation. The change in the perturbation of the propagating THz wave could lead to a definite phase shift. Thus, by applying different bias voltages to the 2DEG with a metal pad, we can control the carrier concentration of the 2DEG to achieve conversion between the 0 and 1 states, realizing a change in the phase manipulation of the transmitting terahertz wave.

Based on this mechanism, we set up a meta-atom array with multiple meta-atoms. Each meta-atom at a certain distance can individually exhibit the perturbation states through different bias voltages, and the perturbations can superimpose on each other. More importantly, perturbations with different intensities are distributed at different positions of the transmission line, bringing about a nonlinear superposition. As depicted in fig. 1, each meta-atom of the meta-atom array is coded with binary code sequences to convert it between the 0 and 1 states; thus, various combinations of the states of all meta-atoms will cause precise phase shifting of the terahertz wave. Hence, we demonstrate a multichannel field perturbation coding 2DEG meta-chip controlled by programing binary codes. Benefiting from this phase manipulation mechanism of local resonant coding perturbation, phase manipulation with different precisions from 2° to 5° is observed from 0.26 to 0.27 THz. Compared with the traditional terahertz metamaterial phase manipulation device, our MPCM demonstrates high-precision phase manipulation with high transmission efficiency and low amplitude fluctuations. Moreover, it has excellent scalability and compatibility for terahertz integrated communications, imaging and radar systems.

Results

Perturbation of the electromagnetic field by single 2DEG meta-atoms.

The perturbation of the electromagnetic field within 2DEG meta-atoms can be demonstrated by the surface current and electromagnetic field distributions. Therefore, to extract persuasive information regarding the phase manipulation characteristics of the MPCM, we first analyzed a single meta-atom field perturbation coding 2DEG meta-chip (SPCM), as shown in fig. 2. Its schematic diagram is shown in fig. 2a, where the blue is the SiC substrate, the yellow is the gold, and the red area in the center is the 2DEG. For comparison, three conditions are included: the bare on-chip microstrip line structure without any

meta-atoms (see fig. 2b, 2e, 2h); the meta-chip with a single meta-atom accompanied by a high carrier concentration of the 2DEG (see fig. 2c, 2f, 2i); and the meta-chip with a single meta-atom accompanied by a low carrier concentration of the 2DEG (see fig. 2d, 2g, 2j).

The distributions of the transient surface current in these three conditions are shown in fig. 2b, fig. 2c and fig. 2d, and the corresponding distributions of the electric field are shown in fig. 2e, fig. 2f and fig. 2g, respectively. In these figures, the color of the current indicates different amplitudes of the current, where a redder color means a larger amplitude and a bluer color means a smaller amplitude. In the case of the first condition, the surface current on the on-chip microstrip line flows from both sides to the middle in a local area, which is just a quasi-TEM transmission mode (see fig. 2b). After a meta-atom is introduced, the surface current on the on-chip microstrip line flows towards the meta-atom (see fig. 2c, 2d). Then, electrons accumulate in both metal electrodes on both sides of the gap, forming an electronic stacking with a local resonance. In the case of a high carrier concentration of the 2DEG in the meta-atom, the electron transport capability is strong, so less electronic stacking occurs in both metal electrodes on both sides of the gap (fig. 2c), which leads to the formation of a local electric field between the gap with HCR (see fig. 2f). When the 2DEG is depleted, the carrier concentration of the 2DEG in the meta-atom is lower, and the electron transport capability is weaker. More electrons accumulate in both metal electrodes (fig. 2d), resulting in the local electric field between the gap becoming stronger, which can enhance the local resonance to be a DR (see fig. 2g). We plotted a normalized surface electric field intensity map along the y-axis with the meta-atom as the center (fig. 2k) to more intuitively demonstrate the variation in the local resonance strength at different carrier concentrations of the 2DEG after the introduction of a meta-atom (the maximum surface electric field intensity of the microstrip transmission line was taken as a reference). In the figure, the electric field on the surface of the microstrip transmission line is symmetrically distributed about the y-axis (gray part). After introducing the meta-atom, the original electron distribution is broken. Under the conditions of a high carrier concentration and a low carrier concentration, the local electric field intensity formed at the gap of the meta-atom is approximately 5.2 times and 8 times the maximum electric field intensity in the microstrip transmission line, respectively.

Resonances of different intensities can be formed by meta-atoms with different carrier concentrations. The local resonances have three remarkable characteristics. First, these local resonances do not directly impact the major field of the terahertz wave in the substrate because the propagation mode of the terahertz wave in the microstrip transmission line is the quasi-TEM mode. Thus, most of the energy is concentrated in the GaN substrate between the microstrip line and the grounded metal plate, and the electric field direction is parallel to the z direction (see fig. 2h), while the meta-atom is fabricated on the surface of the GaN substrate, which does not impact the major field of the terahertz wave. Second, although these local resonances do not directly impact the major field of the terahertz wave, the electric field generated by resonance will provide an electric field component Ez (fig. 2i, 2j) in the z direction, thus causing perturbation of the major electric field of the terahertz wave. Moreover, different local resonances, HCR and DR, mean different electric field components Ez, so the perturbation of the major electric field will change with switching between HCR and DR.

This perturbation not only increases the intensity of the Ez component of the electric field but also increases the area of the electric field distribution in the cross section. According to the relation between the relative equivalent permittivity and the electromagnetic field of a microstrip transmission line[42], the relative equivalent permittivity of the microstrip transmission line will be augmented as the intensity of the Ez component and the area of the electric field distribution in the cross section increase. Thus, the phase velocity will decrease as the relative equivalent permittivity of the microstrip transmission line increases. As a consequence, the phase of the terahertz wave will change when perturbation occurs. Moreover, various perturbations can cause different phase shifts.

We compare the perturbation of the main field for high and low carrier concentrations in fig. 2l. The green and red lines represent the average Ez along the propagation direction of the single meta-atom chip under a high carrier concentration and a low carrier concentration, respectively. The black line shows the average Ez along the propagation direction of the microstrip transmission line, which is taken as the normalized standard. The intensity of the HCR to that of the major electric field at a high carrier concentration is slightly smaller than that of the DR at a low carrier concentration. The perturbation of the major electric field shifts the phase of the THz wave. As shown in fig. 2m, where we take the phase of the THz wave in the microstrip transmission line as a reference, in the case of a high carrier concentration of the 2DEG, the HCR brings about a smaller perturbation such that the phase shift from the reference is 7 degrees. When the carrier concentration of the 2DEG decreases, the DR causes a phase shift of approximately 10 degrees.

High-precision phase manipulation of the MPCM.

The above analysis indicates that the local resonance of the meta-atom will perturb the major field of the terahertz wave in the traditional microstrip line, so phase manipulation can be realized by varying the carrier concentration of the 2DEG to tune the strength of the local resonance. After introducing multiple meta-atoms, we can control the local resonance strength generated by different meta-atoms; thus, the superposition of the perturbations will provide more abundant and more precise phase manipulation.

Here, we coded the high concentration 2DEG resonance (HCR) perturbation as “0” and the depleted 2DEG resonance (DR) perturbation as “1”. As a demonstration, we designed a coding 2DEG meta-chip containing 6 meta-atoms with a total of 64 coding states. The state with the code of 000000 is set to the initial state as a reference.Figure 3 (a-c) depicts the electrical field distributions of each meta-atom under three representative coding sequences of “100000”, “111000” and “101111”. The black pattern in the figure represents the electric field distribution in the case of coding sequence “000000”, and all values of the local resonant electric field intensity have been normalized by an arbitrary preset value. Under coding sequence “100000”, the DR perturbation of the first meta-atom leads to a slight electric field intensity enhancement, while the field intensities of the other five meta-atoms remain the same as the initial state, as shown in fig. 3a. With this analysis, coding sequence “111000” can be found to result in electric field intensity variations of the 1st-3rd meta-atoms, while the last three meta-atoms remain unchanged. Similarly, in the case of coding sequence “101111”, the resonance state of the second meta-atom belongs

to HCR perturbation, so the field is the same as that of the initial state; the other meta-atoms have their own slight field changes. Thus, different coding sequences can lead to various electric field intensity distributions, which makes the superposition of the phase shifts of different meta-atoms perform nonlinearly. Therefore, by applying the nonlinearity of the phase superposition, we can obtain different phase shift degrees and phase shift precisions. As shown in fig. 3d, the phase perturbations in the propagation process under the four coding sequences are different. The black line represents the phase perturbation with code “000000” as a reference. Furthermore, the red, blue and green curves represent the perturbations of the phase for the coding sequences of “100000”, “111000” and “101111”, respectively. The figure shows that the three curves have 1, 3 and 5 perturbations, respectively, which correspond to 1, 3 and 5 DRs in the coding sequence. At the same time, every perturbation caused by a DR will have a certain phase shift, and the more perturbations there are, the larger the phase shift will be. The relationship between the number of DRs and the phase shift of the meta-atom in the meta-chip is shown in fig. 3e-f. When the number of DRs is 0, the coding sequences only include “000000”, for which the phase is indicated by a red point. As the number of DRs increases to 1, the number of coding sequences increases to 6: “100000”, “010000”, “001000”, “000100”, “000010” and “000001”, for which the phase is represented by orange points. We can clearly observe that the phases of the 6 coding sequences are different, which indicates the nonlinear relation of the phase shift with different meta-atoms. Similarly, an increase in the number of DRs to 2 leads to 15 coding sequences. In this case, the phases of the 15 coding sequences exhibit different values, indicated by purple points. Based on the above principle, the total six bits of the code correspond to 64 coding sequences, which provide us with plentiful selections of different phase shifts similar to a coding-phase database. We can determine all high-precision phase shift data under different frequencies from this coding-phase database.

Based on the above results, we designed a low-loss and high-precision multichannel field perturbation coding 2DEG meta-chip (MPCM). The simulation results are shown in fig. 3f-j. At a frequency of 0.265 THz, a continuous phase shift with a minimum phase accuracy of 2° and a maximum phase shift of 50° can be realized, and the insertion loss of the chip is less than 4 dB. At 0.260 THz, the continuous phase shift has a maximum of 35°, where the insertion loss is less than 6 dB. At 0.270 THz, the phase shift can reach 60°. According to the results, different working frequencies can have their own phase distribution relation. Therefore, by applying the coding phase, such a single device can work at different frequencies.

Experimental results of the MPCM.

A prototype of the multichannel field perturbation coding 2DEG meta-chip (MPCM) was obtained by following the processing of a GaN-HEMT. As shown in fig. 4, an epitaxial layer of AlGaN/GaN was grown on a SiC substrate by metal organic chemical vapor deposition (MOCVD) in the first step. After removing oil stains and other impurities, such as metal ions, by the standard cleaning process for HEMTs, a process combining photolithography with excessive etching was used to etch away the zones that did not include the active regions (2DEG regions). Next, several processes, such as photolithography and electron-beam evaporation, were used to fabricate a complex metal layer of Ti/Al/Ni/Au on one side of the active regions. Then, after a high-temperature rapid annealing process at 900°C in nitrogen, the

complex metal layer was lifted off to form an ohmic contact with the 2DEG for negative electrodes. Next, a Ni/Au layer was fabricated on the other side of the active regions by precise electron-beam lithography, forming a Schottky contact for positive electrodes after the lift-off process. Finally, through photolithography, electron-beam evaporation and lift-off processes, a Ni/Au layer was fabricated for accurate connection of the ohmic contact and Schottky contact, forming the whole structure of the 2DEG meta-atom.

As a demonstration, the manufactured 6-channel 2DEG meta-chip is shown in fig. 5e and f. Next, a metallic cavity composed of an input/output rectangular waveguide chip loading area and a control circuit was designed to package this meta-chip, as shown in fig. 5a-c. The control circuit is based on the Rogers 5880, which provides the coding external bias voltage input. Each meta-atom is connected to the pads on the Rogers 5880 by gold bond wires. The external coding control voltage can be loaded on the meta-atom through the Rogers 5880 to realize different coding sequences for the meta-array. Figure 5d demonstrates the whole inner structure. The whole physical process can be described as 3 phases: In the 1^{st} phase, after inputting a terahertz wave to the rectangular waveguide, the E-plane waveguide-microstrip probe can couple the terahertz wave from the rectangular waveguide to the microstrip line. In the 2^{nd} phase, the terahertz wave propagates through the meta-atoms while the external coding voltages are loaded, and a phase shift is induced. In the last phase, the terahertz wave is coupled to the rectangular waveguide and output to the THz detector. A vector network analyzer was utilized to test the packaged device.

The results of the experiment are shown in fig. 6, where fig. 6a, b and c shows the relation diagram between the number of DRs and the phase shift of the meta-atoms at 0.265 THz, 0.260 THz and 0.270 THz, respectively. The phase shift increases with increasing number of DRs of the meta-atoms, consistent with the simulation. Figure 6d, e and f shows the phase shift and insertion loss for different coding sequences at 0.265 THz, 0.260 THz, and 0.270 THz, respectively. At 0.265 THz, we can obtain a total phase shift of over 50° with an insertion loss of approximately 6 dB. In the same way, at 0.260 THz, a total phase shift of over 30° and an insertion loss of less than 7 dB can be achieved. Moreover, at 0.270 THz, we realize a total phase shift of up to 55° with an insertion loss of approximately 8dB.

Further, by applying the principle that different coding sequences correspond to different phase shifts, we can select appropriate coding sequences to design what kind of chip we need. As shown in fig. 6g, the designed multichannel field perturbation coding 2DEG meta-chip possesses a high phase shift precision of 5°, in which the total phase shift can reach 50 degrees with a low insertion loss of approximately 6 dB. In addition, the chip phase shift precision can reach 2° at 0.260 THz, and a phase shift precision of 4° is provided at 0.270 THz. Tables 1-3 show the coding sequences at (Table 1) 265 GHz, (Table 2) 260 GHz, and (Table 3) 270 GHz, which include the phase shift error and insertion loss in each coding state. We finally determine that the average phase shift error is only 0.35° and the average insertion loss is as low as 6.14 dB at 265 GHz. In addition, an average phase shift error of 0.23° and an average insertion loss of 6.04 dB are achieved at 260 GHz; the values obtained at 270 GHz are 0.46° and 8.08 dB. As a

consequence, the chip that we designed not only has a high phase shift precision but also ensures sufficiently low phase shift error and insertion loss.

In summary, based on combining meta-atom perturbation resonance and the electronic transport characteristics of a 2DEG, we have designed a multichannel field perturbation coding 2DEG meta-chip, wherein, by digitally controlling the external coding voltages, high-accuracy phase manipulation of a THz wave can be achieved. Both the simulation and experimental results show that phase manipulation with different precisions from 2° to 5° is obtained from 0.26 to 0.27 THz. The average phase error is only 0.36°, the average transmittance is -6.75 dB, and the maximum root mean square of the transmittance is 0.36 dB, demonstrating high-precision phase manipulation with high transmission efficiency and low amplitude fluctuations. Furthermore, previous contributions inform us that the 2DEG-based magnitude modulator possesses a high modulation rate. Therefore, this on-chip digital coding control has excellent scalability and compatibility for terahertz integrated systems.

Declarations

Acknowledgements

This work is supported by the The National Key Research and Development Program of China under Contract No. 2018YFB1801503；National Natural Science Foundation of China under Contract Nos. 61931006, 61921002 and 61771327.

Author contributions

Hongxin Zeng[&]；Huajie Liang[&]；Ziqiang Yang*；Yaxin Zhang* conceived the idea of the multi-channel field perturbation coding 2DEG meta-chip.

Competing interests

The authors declare no competing interests.

References

1. Siegel, P. H. Terahertz technology. *IEEE Trans. Microw. Theory Tech.* **50**, 910–928 (2002).
2. Federici, J. F. *et al.* THz imaging and sensing for security applications - Explosives, weapons and drugs. *Semicond. Sci. Technol.* **20**, (2005).
3. Sun, S., He, Q., Hao, J., Xiao, S. & Zhou, L. Electromagnetic metasurfaces: physics and applications. *Adv. Opt. Photonics* **11**, 380 (2019).
4. Wang, L. *et al.* A review of THz modulators with dynamic tunable metasurfaces. *Nanomaterials* **9**, (2019).
5. Chen, Z. *et al.* A survey on terahertz communications. *China Commun.* **16**, 1–35 (2019).

6. Tonouchi, M. Cutting-edge terahertz technology. *Nat. Photonics* **1**, 97–105 (2007).
7. Savinov, V., Fedotov, V. A., Anlage, S. M., De Groot, P. A. J. & Zheludev, N. I. Modulating Sub-THz radiation with current in superconducting metamaterial. *Phys. Rev. Lett.* **109**, 1–5 (2012).
8. Liu, A. Q., Zhu, W. M., Tsai, D. P. & Zheludev, N. I. Micromachined tunable metamaterials: A review. *J. Opt. (United Kingdom)* **14**, (2012).
9. Zheludev, N. I. & Kivshar, Y. S. From metamaterials to metadevices. *Nat. Mater.* **11**, 917–924 (2012).
10. Mittleman, D. M. Frontiers in terahertz sources and plasmonics. *Nat. Photonics* **7**, 666–669 (2013).
11. Watts, C. M. *et al.* Terahertz compressive imaging with metamaterial spatial light modulators. *Nat. Photonics* **8**, 605–609 (2014).
12. Dhillon, S. S. *et al.* The 2017 terahertz science and technology roadmap. *J. Phys. D. Appl. Phys.* **50**, (2017).
13. Guo, J. *et al.* Reconfigurable Terahertz Metasurface Pure Phase Holograms. *Adv. Opt. Mater.* **7**, 1–7 (2019).
14. Chen, H. T. *et al.* Active terahertz metamaterial devices. *Nature* **444**, 597–600 (2006).
15. Chen, H. T., O'Hara, J. F., Azad, A. K. & Taylor, A. J. Manipulation of terahertz radiation using metamaterials. *Laser Photonics Rev.* **5**, 513–533 (2011).
16. Singh, R., Al-Naib, I. A. I., Koch, M. & Zhang, W. Sharp Fano resonances in THz metamaterials. *Opt. Express* **19**, 6312 (2011).
17. Yao, Y. *et al.* Broad electrical tuning of graphene-loaded plasmonic antennas. *Nano Lett.* **13**, 1257–1264 (2013).
18. Zhang, Y. *et al.* Gbps terahertz external modulator based on a composite metamaterial with a double-channel heterostructure. *Nano Lett.* **15**, 3501–3506 (2015).
19. Jessop, D. S. *et al.* Graphene based plasmonic terahertz amplitude modulator operating above 100 MHz. *Appl. Phys. Lett.* **108**, (2016).
20. Kim, T. T. *et al.* Amplitude Modulation of Anomalously Refracted Terahertz Waves with Gated-Graphene Metasurfaces. *Adv. Opt. Mater.* **6**, 1–7 (2018).
21. Zhao, Y. *et al.* High-Speed Efficient Terahertz Modulation Based on Tunable Collective-Individual State Conversion within an Active 3 nm Two-Dimensional Electron Gas Metasurface. *Nano Lett.* **19**, 7588–7597 (2019).
22. Chen, H. T. *et al.* A metamaterial solid-state terahertz phase modulator. *Nat. Photonics* **3**, 148–151 (2009).
23. Manceau, J. M., Shen, N. H., Kafesaki, M., Soukoulis, C. M. & Tzortzakis, S. Dynamic response of metamaterials in the terahertz regime: Blueshift tunability and broadband phase modulation. *Appl. Phys. Lett.* **96**, 2008–2011 (2010).
24. Shen, N. H. *et al.* Optically implemented broadband blueshift switch in the terahertz regime. *Phys. Rev. Lett.* **106**, (2011).

25. Lee, S. H. *et al.* Switching terahertz waves with gate-controlled active graphene metamaterials. *Nat. Mater.* **11**, 936–941 (2012).
26. Urade, Y. *et al.* Dynamically Babinet-invertible metasurface: a capacitive-inductive reconfigurable filter for terahertz waves using vanadium-dioxide metal-insulator transition. *Opt. Express* **24**, 4405 (2016).
27. Ji, Y.-Y., Fan, F., Chen, M., Yang, L. & Chang, S.-J. Terahertz artificial birefringence and tunable phase shifter based on dielectric metasurface with compound lattice. *Opt. Express* **25**, 11405 (2017).
28. Zhou, Z., Wang, S., Yu, Y., Chen, Y. & Feng, L. High performance metamaterials-high electron mobility transistors integrated terahertz modulator. *Opt. Express* **25**, 17832 (2017).
29. Zhao, Y. *et al.* Dynamic Photoinduced Controlling of the Large Phase Shift of Terahertz Waves via Vanadium Dioxide Coupling Nanostructures. *ACS Photonics* **5**, 3040–3050 (2018).
30. Zhang, Y. *et al.* Large phase modulation of THz wave via an enhanced resonant active HEMT metasurface. *Nanophotonics* **8**, 153–170 (2018).
31. Hu, Y. *et al.* Ultrafast Terahertz Frequency and Phase Tuning by All-Optical Molecularization of Metasurfaces. *Adv. Opt. Mater.* **7**, 1–10 (2019).
32. Kakenov, N., Ergoktas, M. S., Balci, O. & Kocabas, C. Graphene based terahertz phase modulators. *2D Mater.* **5**, (2018).
33. Yang, C.-S. *et al.* Voltage-controlled liquid-crystal terahertz phase shifter with indium–tin–oxide nanowhiskers as transparent electrodes. *Opt. Lett.* **39**, 2511 (2014).
34. Li, L. *et al.* Electromagnetic reprogrammable coding-metasurface holograms. *Nat. Commun.* **8**, 1–7 (2017).
35. Li, L. *et al.* Machine-learning reprogrammable metasurface imager. *Nat. Commun.* **10**, (2019).
36. Li, L. *et al.* Intelligent metasurface imager and recognizer. *Light Sci. Appl.* **8**, (2019).
37. Fu, X., Yang, F., Liu, C., Wu, X. & Cui, T. J. Terahertz Beam Steering Technologies: From Phased Arrays to Field-Programmable Metasurfaces. *Adv. Opt. Mater.* **8**, 1–22 (2020).
38. Fu, X. & Cui, T. J. Recent progress on metamaterials: From effective medium model to real-time information processing system. *Prog. Quantum Electron.* **67**, 100223 (2019).
39. Li, L. & Cui, T. J. Information metamaterials - From effective media to real-time information processing systems. *Nanophotonics* **8**, 703–724 (2019).
40. Wan, X. *et al.* Multichannel direct transmissions of near-field information. *Light Sci. Appl.* **8**, (2019).
41. Zhao, J. *et al.* Programmable time-domain digital-coding metasurface for non-linear harmonic manipulation and new wireless communication systems. *Natl. Sci. Rev.* **6**, 231–238 (2019).
42. Dukes, J. M. C. An investigation into some fundamental properties of strip transmission lines with the aid of an electrolytic tank. *Proc. IEE - Part B Radio Electron. Eng.* **103**, 319–333 (1956).

Table

Table 1. Measured data with a precision of 5° at 265 GHz

State	Coding sequence	Phase (°)	Error (°)	Loss (dB)
1	000000	0.0	0	-6.33
2	001000	-5.2	0.2	-6.46
3	010000	-10.0	0	-6.28
4	010100	-14.8	0.2	-6.30
5	001010	-19.5	0.5	-6.25
6	001001	-25.4	0.4	-5.97
7	011100	-31.3	1.3	-6.16
8	010011	-34.8	0.2	-5.70
9	111010	-40.1	0.1	-6.14
10	101111	-45.1	0.1	-5.98
11	111101	-50.8	0.8	-5.96
Average phase error			0.35	——
Average loss			——	-6.14

Table 2. Measured data with a precision of 2° at 260 GHz

State	Coding sequence	Phase (°)	Error (°)	Loss (dB)
1	000000	0.0	0	-6.62
2	100000	-3.0	1	-6.39
3	000100	-4.2	0.2	-6.12
4	101000	-5.5	0.5	-6.41
5	100010	-8.1	0.1	-6.51
6	001100	-9.8	0.2	-5.75
7	110100	-12.2	0.2	-5.84
8	010001	-14.2	0.2	-5.84
9	101010	-16.0	0	-6.10
10	101001	-18.2	0.2	-6.43
11	001101	-20.0	0	-6.08
12	011101	-22.1	0.1	-5.81
13	110011	-24.1	0.1	-5.57
14	100111	-26.2	0.2	-6.06
15	101111	-27.6	0.4	-5.26
16	111011	-30.3	0.3	-5.81
Average phase error			0.23	——
Average loss			——	-6.04

Table 3. Measured data with a precision of 4° at 270 GHz

State	Coding sequence	Phase (°)	Error (°)	Loss (dB)
1	000000	0.0	0.0	-8.44
2	000001	-4.4	0.4	-8.51
3	001000	-8.4	0.4	-8.20
4	100100	-11.4	0.6	-8.01
5	110000	-17.0	1.0	-7.87
6	000110	-19.9	0.1	-8.41
7	001001	-23.3	0.7	-8.37
8	100011	-28.0	0.0	-8.38
9	010011	-32.0	0.0	-7.85
10	001110	-34.9	1.1	-7.90
11	110011	-39.8	0.2	-7.70
12	101111	-45.2	1.2	-7.76
13	111011	-48.7	0.7	-7.65
Average phase error			0.49	——
Average loss			——	-8.08

Figures

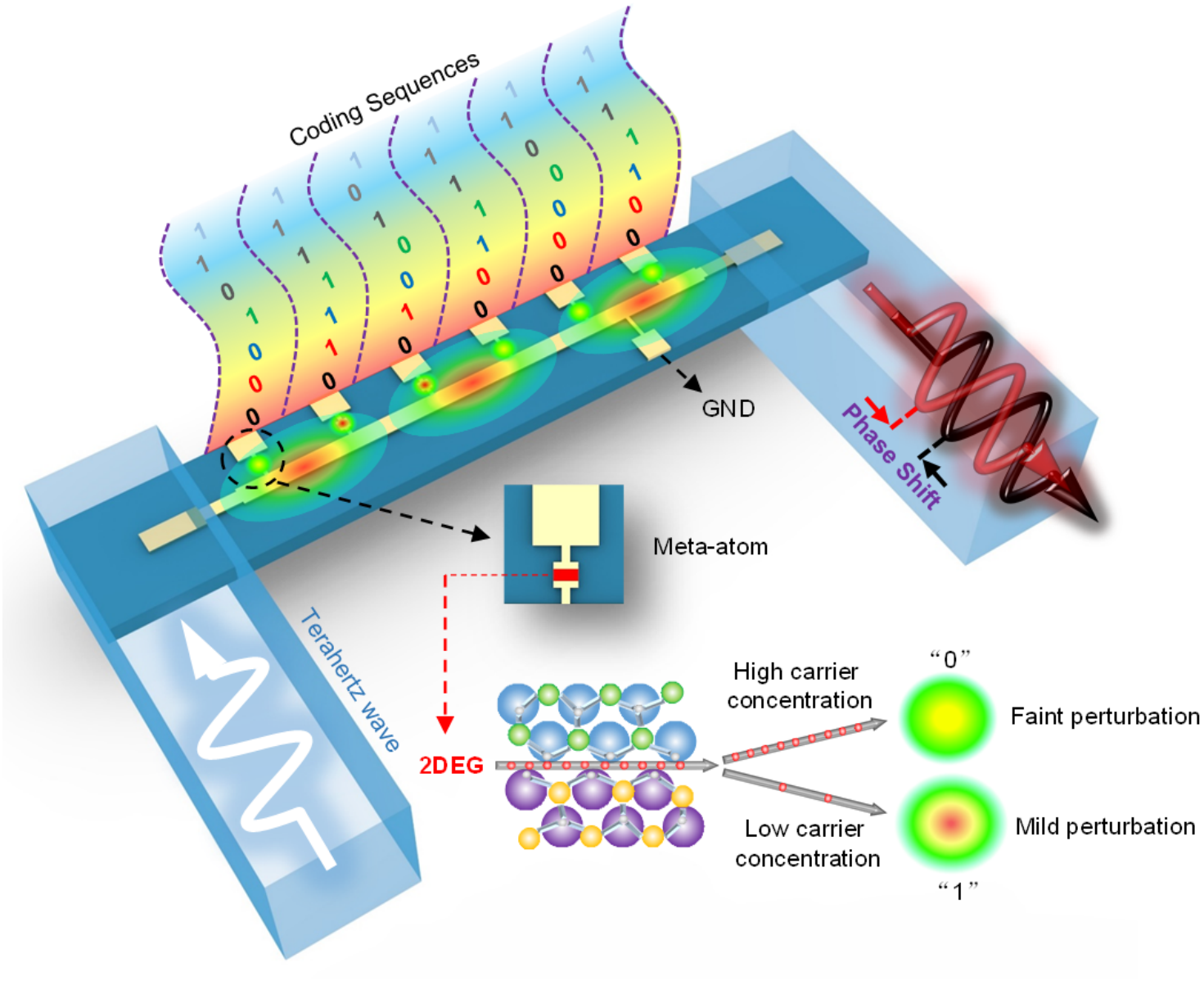

Figure 1

MPCM architecture and its high-precision terahertz phase manipulation function.

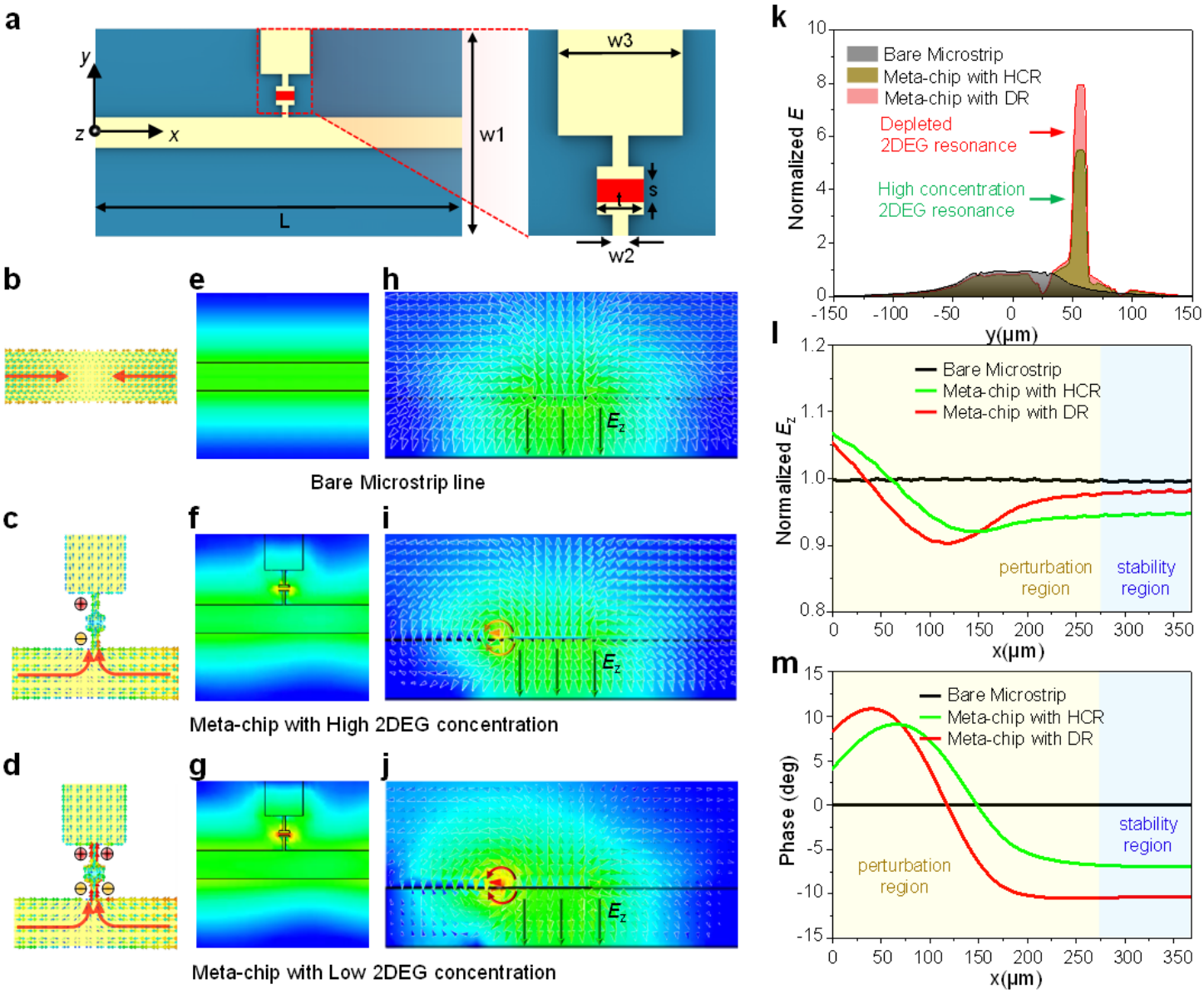

Figure 2

Electric field perturbation and phase manipulation of the MPCM. a-c Perturbation distribution of the electric field on the MPCM encoded with 000000, (a) 100000, (b) 111000, and (c) 101111. d Phase perturbations on the MPCM encoded with 000000, 100000, 111000, and 101111.e-g Phase shift as a function of the number of DRs (encoded as "1") at (a) 265 GHz, (b) 260 GHz, and (c) 270 GHz. h-j Continuous phase shift and transmittance of the 64 coding states from the coding sequence 000000 to 111111 at (d) 265 GHz, (e) 260 GHz, and (f) 270 GHz.

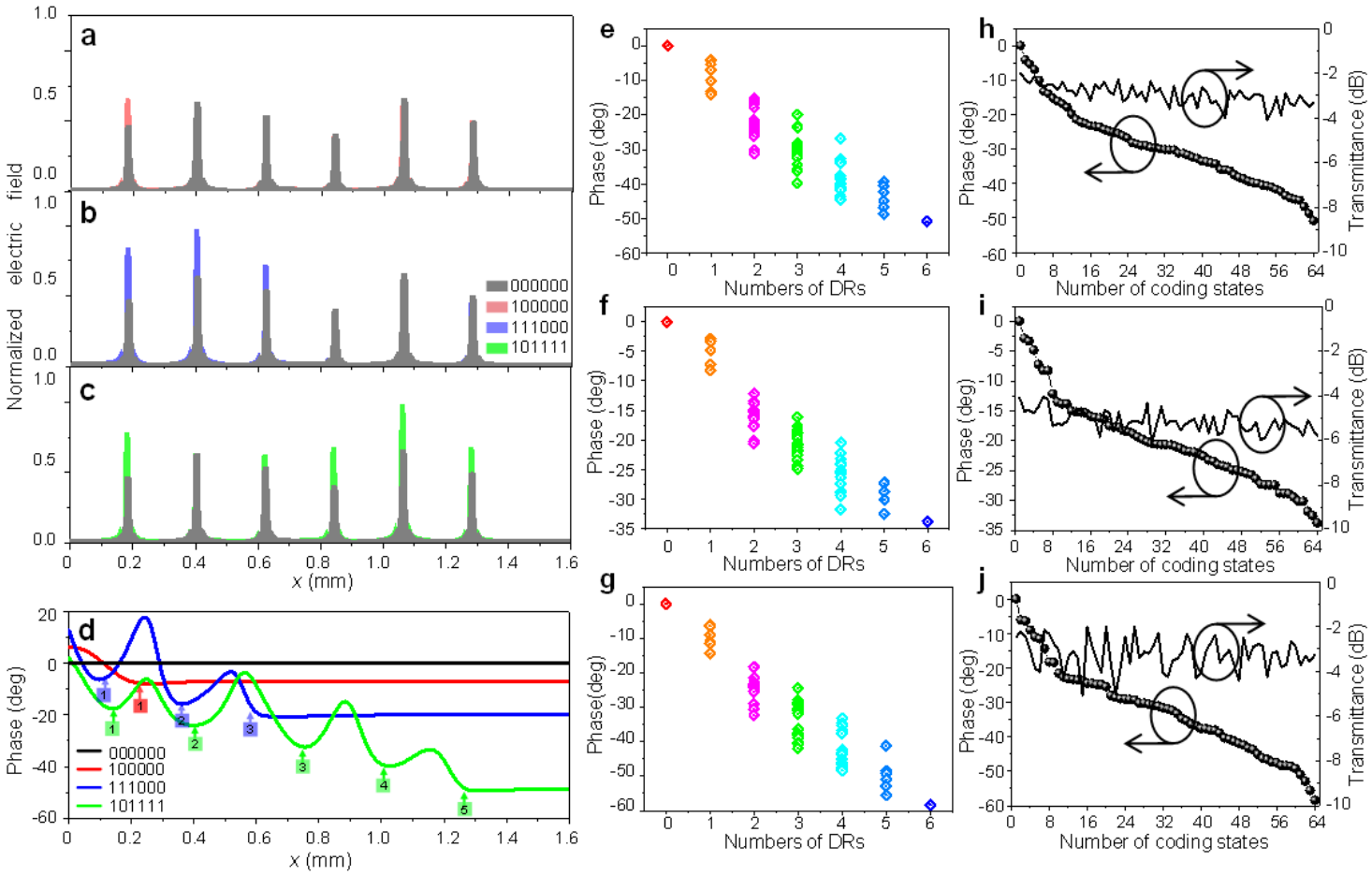

Figure 3

Electric field perturbation and phase manipulation of the MPCM. a-c Perturbation distribution of the electric field on the MPCM encoded with 000000, (a) 100000, (b) 111000, and (c) 101111. d Phase perturbations on the MPCM encoded with 000000, 100000, 111000, and 101111.e-g Phase shift as a function of the number of DRs (encoded as "1") at (a) 265 GHz, (b) 260 GHz, and (c) 270 GHz. h-j Continuous phase shift and transmittance of the 64 coding states from the coding sequence 000000 to 111111 at (d) 265 GHz, (e) 260 GHz, and (f) 270 GHz.

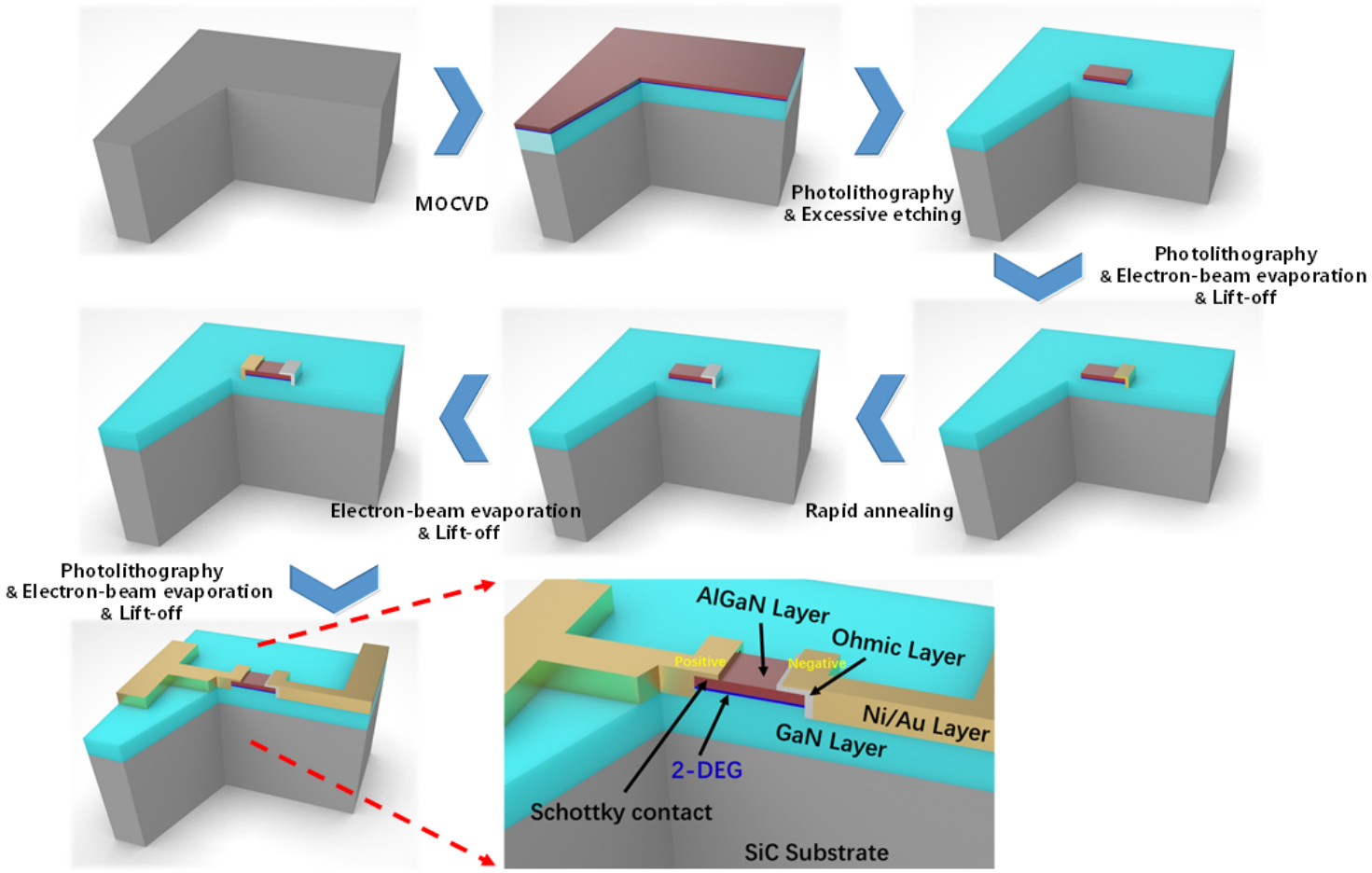

Figure 4

Brief process flowchart of the fabrication of a GaN-HEMT and meta-atoms

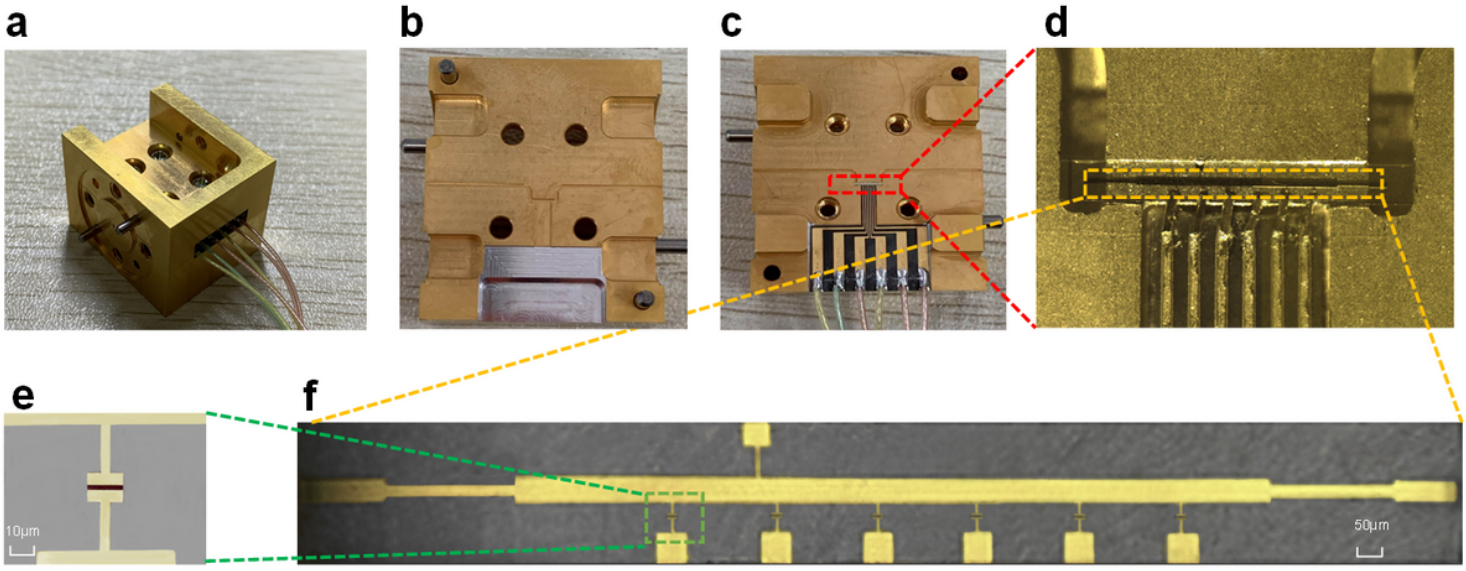

Figure 5

MPCM photo and assembled test cavity. a-d Photographic image of the fabricated test cavity containing the MPCM. The (a) entire test cavity is composed of (b) the upper cavity and (c) the lower cavity. (d) The lower cavity is used to hold the MPCM and layout of the feeding circuit. e Optical micrograph of a meta-atom. f Optical micrograph of the MPCM.

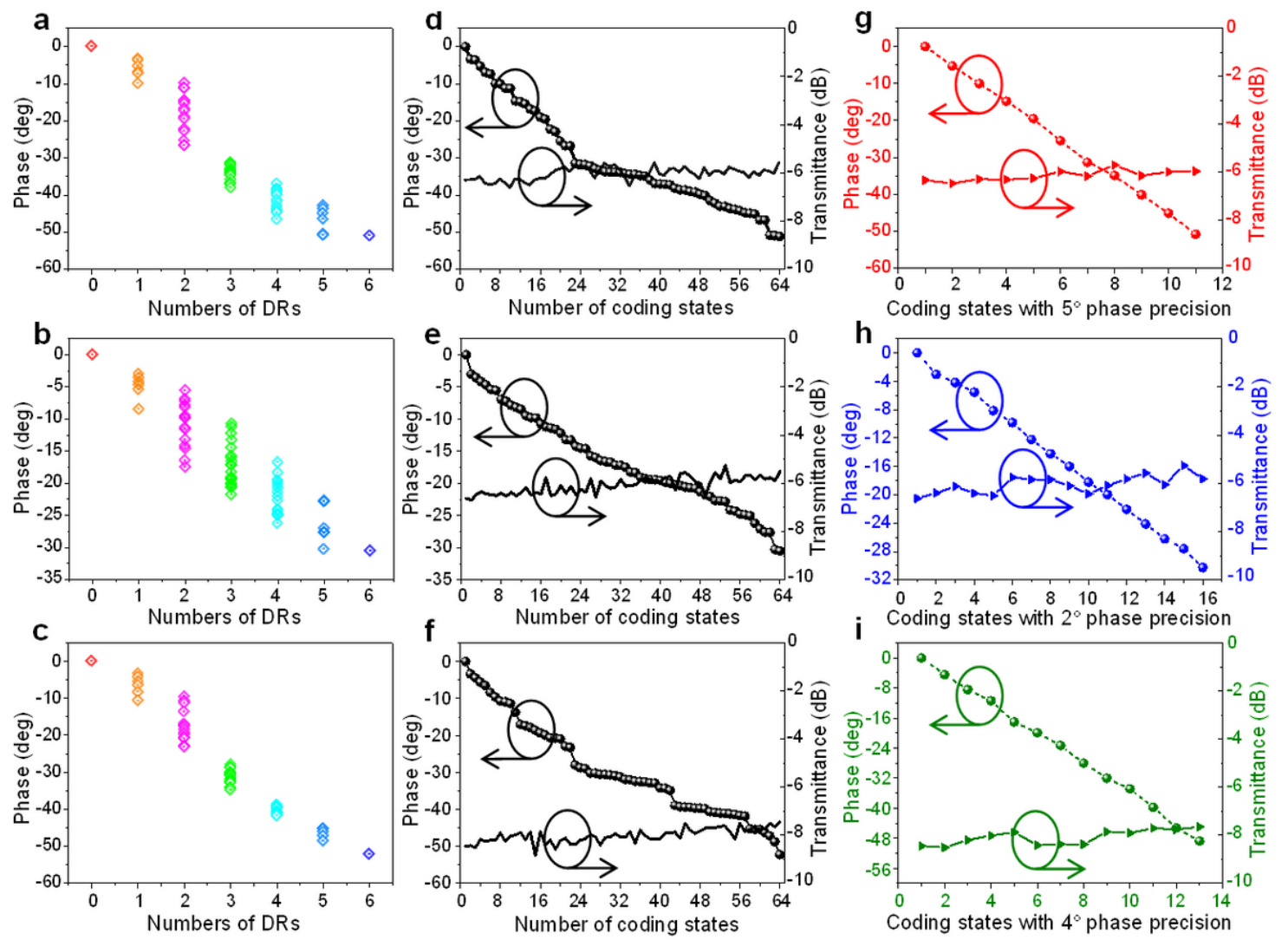

Figure 6

Measurement results of MPCM phase manipulation and transmittance. a-c Phase shift as a function of the number of DRs (encoded as "1") at (a) 265 GHz, (b) 260 GHz, and (c) 270 GHz. d-f Phase shift and transmittance of the 64 coding states from coding sequence 000000 to 111111 at (d) 265 GHz, (e) 260 GHz, and (f) 270 GHz. g-i High-precision and -linearity phase manipulation characteristics. (g) Phase shift characteristics with a precision of 5° at 265 GHz, (h) phase shift characteristics with a precision of 2° at 260 GHz, and (i) phase shift characteristics with a precision of 4° at 270 GHz.